High-pressure phase transition of a natural pigeonite

Matteo Alvaro,[1,*] Fabrizio Nestola,[2] Tiziana Boffa Ballaran,[3] Fernando Cámara,[4] M. Chiara Domeneghetti,[1] and Vittorio Tazzoli[1,4]

[1]Dipartimento di Scienze della Terra, Università di Pavia, Via Ferrata 1, I-27100 Pavia, Italy
[2]Dipartimento di Geoscienze, Università di Padova, Via Giotto 1, I-35137 Padova, Italy
[3]Bayerisches Geoinstitut, Universität Bayreuth, Universitätstraße 37, D-95440 Bayreuth, Germany
[4]C.N.R.–Istituto di Geoscienze e Georisorse, Unità di Pavia, Via Ferrata 1, I-27100 Pavia, Italy

Abstract

High-pressure and room-temperature single-crystal X-ray diffraction (XRD) studies have been performed on crystals of a natural pigeonite sample with composition ca. $Wo_{10}En_{43}Fs_{47}$ using diamond-anvil cells. The unit-cell parameters were determined at 18 different pressures up to about 6 GPa. A first-order $P2_1/c$-$C2/c$ phase transition was found between 3.5 and 3.6 GPa, associated with the disappearance of the b-type reflections ($h + k$ = odd) and a strong discontinuity (about 1.7%) in the unit-cell volume. At the transition, a small hysteresis (~0.3 GPa) was observed. A third-order Birch-Murnaghan equation of state (BM3-EoS) fit to the 10 P-V data of the low-P phase yielded $V_0 = 431.93(2)$ Å^3, K_{T0} = 96.8(8) GPa and $K' = 8.5(6)$. A second-order Birch-Murnaghan EoS fit to the 8 P-V data (between 3.6 and 6 GPa) of the $C2/c$ high-P phase yielded $V_0 = 423.6(1)$ Å^3 and $K_{T0} = 112.4(8)$, indicating that the high-P $C2/c$ phase is significantly stiffer than the low-P phase.

In a separated experiment with crystals of the same sample, intensity data were collected and crystal structures were refined at 13 pressures up to 9.4 GPa. The M1-O and M2-O mean bond lengths of the low-P $P2_1/c$ phase decrease by 0.7 and 2.1%, respectively. The two non-equivalent A and B tetrahedral chains become more kinked with pressure, with a reduction of their angle by 2.2 and 5.1%, respectively. At the transition the A-chain changes sense of rotation and both chains become equivalent and more kinked, with a further reduction of their angle by 2.5% up to 9.4 GPa.

Strain calculations have been performed and the evolution of the spontaneous strain and the order parameter variation with pressure are discussed, considering geometrical parameters of the structure and comparing our results with the available data for other compositions.

Keywords: Pigeonite, high-pressure, single crystal XRD, diamond-anvil cell, phase transition, spontaneous strain

Introduction

Mg-rich clinopyroxenes (CPXs) are among the most abundant phases of the Earth's upper mantle, and therefore the knowledge of their structural and thermodynamic properties is crucial in constraining the geodynamic models in which they are involved. In particular, low-Ca pyroxenes show $P2_1/c$-$C2/c$ high-pressure and high-temperature phase transitions strongly dependent upon composition (Angel et al. 1992; Ross and Reynard 1999; Tribaudino et al. 2002; Cámara et al. 2002; Nestola et al. 2004). The HT and HP $C2/c$ clinopyroxenes are structurally different, as the tetrahedral chains are extended in the HT $C2/c$ structure and strongly kinked in the HP $C2/c$ structure (Angel et al. 1992; Angel and Hugh-Jones 1994; Hugh-Jones and Angel 1994; Hugh-Jones et al. 1994; Arlt et al. 1998; Arlt and Angel 2000). The substitution of Fe in $MgSiO_3$ clinopyroxenes induces a decrease in the transition pressure P_c and a disappearance of hysteresis (Hugh-Jones et al. 1994; Ross and Reynard 1999). Also the substitution of Ca causes a significant decrease of P_c (Tribaudino et al. 2001; Nestola et al. 2004) and affects the thermodynamic character of

the transition (Tribaudino et al. 2001). Arlt et al. (1998) have suggested that the transition pressure of the $P2_1/c$ to HP $C2/c$ phase transformation is not exclusively controlled by the ionic radii of the M1 and M2 cations, but that an additional stabilization of the HP $C2/c$ structure may arise from crystal field effects when the clinopyroxene contains Cr^{2+} and/or Fe^{2+}. Natural pigeonites may be considered clinopyroxenes with mixed compositions along the clinoferrosilite-clinoenstatite join containing small amounts of Ca. This Ca substitution may be crucial in determining the high-pressure behavior of pigeonite, however, with respect to the $(Mg,Fe)SiO_3$ clinopyroxenes, since no stabilization energy from crystal field effect can be expected for the Ca atom.

In this study, we have performed single-crystal high-pressure X-ray diffraction experiments on pigeonite sample BTS-308, previously studied at high-T and room pressure by Cámara et al. (2002) and Domeneghetti et al. (2005), with composition ca. $Wo_{10}En_{43}Fs_{47}$, to constrain the simultaneous effect of Ca and Fe^{2+} substitution into the clinoenstatite structure. Moreover, we have calculated the lattice strain associated with the $P2_1/c$-$C2/c$ high-pressure phase transition to constrain its thermodynamic behavior in the framework of the Landau theory.

---

* E-mail: matteo_alvaro@dst.unipv.it

EXPERIMENTAL METHODS

Samples

Three twin and inclusion-free single crystals of pigeonite from the Paranà (Brazil) rhyodacite BTS-308 sample (Secco et al. 1988) were selected for this study.

These crystals, labeled BTS-308 N.1, N.2, and N.3 have a composition slightly Fe-richer than that of BTS-308 crystals studied by Domeneghetti et al. (2005) i.e., $^{M2}(Ca_{0.19}Mg_{0.09}Fe_{0.69}Mn_{0.03})^{M1}(Mg_{0.75}Fe_{0.23}Fe^{3+}_{0.01}Ti_{0.01})^{T}(Si_{1.97}Al_{0.03})O_2$, maximum and minimum size between 180 and 50 μm. Preliminary analysis by X-ray diffraction shows that the samples have similar unit-cell parameters (within the e.s.d. values) and sharp diffraction profiles. The presence of exsolved augite lamellae has been excluded by rocking profiles, in agreement with what already observed by Pasqual et al. (2000) in their TEM study.

High-pressure X-ray diffraction

In a first experiment, carried out at the Bayerisches Geoinstitut (Bayreuth), unit-cell parameters were determined by XRD at 18 different pressures up to about 6 GPa using a HUBER four-circle diffractometer and the SINGLE software (Ralph and Finger 1982; Angel et al. 2000). The BTS-308 N.1 crystal was loaded in a BGI-type diamond anvil cell (DAC, Allan et al. 1996), using a steel gasket (T301), pre-indented to a thickness of 110 μm and with a hole of 300 μm in diameter. A single crystal of quartz was used as an internal diffraction pressure standard (Angel et al. 1997) and a 4:1 mixture of methanol:ethanol was used as hydrostatic pressure medium. Unit-cell parameters were determined at high pressure by the method of eight-position diffracted-beam centering (King and Finger 1979; Angel et al. 2000). The unit-cell parameters data are reported in Table 1.

In a second experiment, carried out at the Dipartimento di Geoscienze (University of Padova), XRD intensity data were collected at 11 different pressures up to 9.4 GPa using a STOE Stadi 4 single-crystal diffractometer equipped with a CCD detector (graphite monochromated Mo$K\alpha$ radiation, Oxford Diffraction) and a ETH-type DAC (Miletich et al. 2000). A preliminary data collection performed on the randomly oriented crystal N.2 showed that only few independent reflections could be collected, which resulted in large uncertainties on some interatomic distances parallel to [100] during the structure refinement. Therefore, a second single crystal of BTS-308 sample, i.e., crystal BTS-308 N.3, with a different orientation was loaded into the same DAC assemblage (see for reference Johnson 2007). This crystal was previously oriented on the (112) plane, thinned and polished. A steel gasket (T301), pre-indented to 90 μm and with a hole of 250 μm in diameter and a 16:3:1 mixture of methanol:ethanol:water was used as hydrostatic pressure medium. As the unit-cell volumes measured at ambient conditions on crystals N.1, N.2, and N.3 are in good agreement (with differences less than two e.s.d. values), no pressure standard was used in this second experiment and the internal pressure of each data point was determined using the equation of state calculated from the unit-cell parameters collected for BTS-308 N.1, following the same experimental procedure used in Nestola et al. (2008a).

For each pressure experiment, intensity data were collected in the $5 \leq 2\theta \leq 60°$ range using a 0.2° ω-scan and an exposure time of 60 s per frame. The sample-detector distance was 60 mm. The program CrysAlis RED (Oxford Diffraction) was

used to integrate the intensity data, applying the Lorentz-polarization correction. The combined use of X-RED (Stoe and Cie 2001), X-SHAPE (Stoe and Cie 1999), and ABSORB6.0 (Angel 2004) programs was adopted to correct for absorption and also to take into account the effect of gasket shadowing (Angel et al. 2000). The intensity data of the two crystals were used for weighted structure refinement by applying two scale factors, starting from the atomic coordinates of Pasqual et al. (2000). The package SHELX-97 (Sheldrick 1998) was used. Structure refinements were performed in space group $P2_1/c$ for data measured up to 3.15 GPa. Above this pressure, the disappearance of the b-type reflections ($h + k = 2n + 1$) was observed, indicating that a transition to a C centered lattice had occurred. Therefore, the structure refinements of data measured between 3.6 and 9.4 GPa were performed in space group $C2/c$, starting from the atomic coordinates of Nestola et al. (2004). The atomic scattering curves were taken from the *International Tables for X-Ray Crystallography* (Wilson 1995). Neutral vs. ionized scattering factors were refined for O and Si, while ionized scattering factors were used for Fe, Ca, and Mg. A residual electron-density maximum, located 0.5–0.6 Å from the M2 site, was observed in the difference-Fourier map for all the crystals at all pressures during the experiments. The same feature had previously been observed by Cámara et al. (2002) and Domeneghetti et al (2005) in another BTS-308 pigeonite crystal, and by Tribaudino and Nestola (2002) in two synthetic $P2_1/c$ clinopyroxene samples with compositions $Di_{15}En_{85}$ and $Di_{23}En_{77}$. As suggested by these authors, this residual electron density is due to positional disorder of Ca at the M2 site. A M21 split position, with the atomic coordinates of the residual (ca. $x = 0.25$, $y = 0.08$, $z = 0.26$), was then introduced in the structure refinements with a soft constraint based on the M2-M21 distance observed in the difference-Fourier map. In the structure refinement, only the atomic displacement parameters of the M1 and M2 sites were treated as anisotropic (see deposit items). Structure refinements carried out in $P2_1/c$ symmetry with the M21 split model resulted in an improvement of the agreement factor with respect to the non-split model. In contrast, the M21 split model was not applied in the $C2/c$ structure refinements as no further improvement was observed. For all high-pressure data, the Mg and Fe site occupancies of the M1 and M2 sites were constrained to those obtained for crystal N.2, for which the structure refinement was performed using the data collected with the crystal in air. Unit-cell parameters and details of the structure refinements are reported in Table 2; fractional coordinates and atomic displacement parameters are reported in Table 3. Selected bond lengths, polyhedral volumes, and further geometrical parameters are reported in Tables 4a and 4b. Lists of observed and calculated structure factors have been deposited[1].

RESULTS AND DISCUSSION

Phase transition, elastic behavior, and equation of state

The variation of the unit-cell parameters as a function of pressure is shown in Figure 1. All the cell parameters decrease following a non-linear trend up to 3.567 GPa (Table 1). In particular, between room pressure and 3.567 GPa, both a and c parameters decrease by 1.1% (Figs. 1a and 1c), b and $a\sin\beta$ by 0.9 and 0.7%, respectively (Figs. 1b and 1e), and the unit-cell volume by about 3.3% (Fig. 1f). Between 3.567 and 3.603 GPa, all the cell parameters undergo a sharp discontinuity: a, c, and β of about -1.1, -2.5, and -3.3%, respectively, b and $a\sin\beta$ of about $+0.1$ and $+0.7$%, and the unit-cell volume of about -1.7%. Data collected in decompression show that the hysteresis is small and is about 0.3 GPa (Table 1). The discontinuity represents a strong first-order phase transition, which corresponds to the $P2_1/c \leftrightarrow C2/c$ symmetry change as supported by the simultaneous sudden disappearance at this pressure of the $h + k = 2n + 1$ reflections, which violate the lattice C-centering. The same behavior was observed for clinoenstatite, $Mg_2Si_2O_6$ (Angel and Hugh-Jones 1994;

TABLE 1. Unit-cell parameters at the different pressure values, obtained on the crystal BTS-308 N.1

P (GPa)	a (Å)	b (Å)	c (Å)	β (°)	V (Å³)
0.00010(1)	9.7087(2)	8.9396(2)	5.2475(1)	108.486(2)	431.93(2)
0.458(4)*	9.6932(7)	8.9227(4)	5.2386(3)	108.382(6)	429.97(4)
1.348(5)*	9.6625(5)	8.8899(3)	5.2234(2)	108.198(4)	426.24(3)
1.929(7)	9.6448(3)	8.8685(3)	5.2137(2)	108.048(2)	424.01(2)
2.437(5)	9.6313(3)	8.8515(4)	5.2062(3)	107.954(3)	422.22(3)
3.014(5)	9.6147(3)	8.8326(3)	5.1977(2)	107.850(2)	420.16(2)
3.496(5)*	9.6016(4)	8.8178(4)	5.1906(2)	107.786(3)	418.46(3)
3.516(6)*	9.6007(4)	8.8180(4)	5.1903(2)	107.783(3)	418.41(3)
3.551(5)	9.6004(4)	8.8164(5)	5.1902(2)	107.779(3)	418.32(3)
3.567(5)*	9.5997(4)	8.8161(4)	5.1898(2)	107.777(3)	418.25(3)
3.536(6)	9.4927(4)	8.8273(3)	5.0618(2)	104.165(3)	411.26(2)
3.603(6)	9.4897(5)	8.8260(5)	5.0607(3)	104.145(4)	411.02(3)
3.627(7)*	9.4892(4)	8.8249(5)	5.0600(3)	104.128(3)	410.91(3)
3.780(6)*	9.4856(3)	8.8202(5)	5.0572(1)	104.088(2)	410.39(2)
3.820(5)	9.4854(2)	8.8190(3)	5.0569(2)	104.079(2)	410.31(2)
4.430(7)	9.4678(2)	8.8030(3)	5.0468(1)	103.913(2)	408.29(2)
5.129(8)	9.4499(3)	8.7845(3)	5.0366(2)	103.751(2)	406.12(2)
6.033(7)	9.4284(3)	8.7620(3)	5.0246(2)	103.578(3)	403.49(2)

Data measured during decompression.

TABLE 2. Unit-cell parameters of crystal BTS-308 N.2, structure refinements results on crystals BTS-308 N.2 and N.3, and order parameter (Q^2, calculated as $\Sigma I_b/\Sigma I_a$*) for crystal BTS-308 N.2

P (GPa)	0.0001	0.047	0.984	1.794	3.167	3.172†	3.587	3.649	6.409†	7.762	9.405
a (Å)	9.749(9)	9.722(8)	9.701(11)	9.659(5)	9.621(6)	9.622(14)	9.518(8)	9.494(6)	9.434(9)	9.402(6)	9.366(17)
b (Å)	8.937(6)	8.941(10)	8.887(9)	8.877(5)	8.827(5)	8.861(14)	8.804(7)	8.818(6)	8.745(8)	8.716(6)	8.682(18)
c (Å)	5.246(5)	5.247(3)	5.226(3)	5.218(2)	5.199(3)	5.181(7)	5.056(4)	5.060(3)	5.014(5)	4.996(6)	4.974(8)
b (°)	108.49(9)	108.50(8)	108.38(11)	108.09(5)	107.82(6)	107.92(13)	104.04(7)	104.11(6)	103.44(9)	103.28(6)	103.09(15)
V (Å³)	433.5(7)	432.5(6)	427.6(7)	425.3(4)	420.3(4)	420.3(1.1)	411.0(6)	410.8(5)	402.3(7)	398.5(4)	394.0(1)
Space group	P2₁/c	P2₁/c	P2₁/c	P2₁/c	P2₁/c	P2₁/c	C2/c	C2/c	C2/c	C2/c	C2/c
Z	4	4	4	4	4	4	4	4	4	4	4
no. of I/σ > 4	662	637	636	636	635	649	376	377	362	355	329
n all‡	983	968	958	969	928	959	472	481	466	459	450
R(merge)	0.973	0.856	0.915	0.18	0.148	0.135	0.381	0.749	0.484	0.168	0.133
GooF	1.1	1.1	1.1	1.2	1.2	1.2	1.2	1.3	1.2	1.1	1.1
R_int (%)§	6.7	8.4	8	8.7	5.4	4.6	6.8	6.6	4.5	5.9	6.9
R_4σ (%)	7.6	9.1	9.9	9.4	7.8	7.7	6.6	7.5	7.4	7.6	8.9
R_W	21.4	19.8	20.3	22.1	16.9	18.8	17.1	20.0	20.4	21.8	24.2
R_all‡	11.4	16.8	16.9	15.3	13.2	13.5	9.3	9.8	10	10.2	11.7
NP‖	62	62	62	62	62	62	34	34	34	34	34
Q²	0.32	0.32	0.34	0.39	0.54	0.55					

Note: Estimated pressures errors 0.05 GPa.
* a-type reflections: $\bar{4}04$, 002, $\bar{8}25$, $\bar{9}33,\bar{6}64$, $\bar{3}33$, and b-type reflections: $\bar{3}04$, $\bar{2}33$, $\bar{8}35$, 102, $\bar{8}33$, $\bar{7}64$.
† Data measured during decompression.
‡ Reflections have not been merged for 2/m Laue group because we used two different data sets.
§ $R_{int} = \Sigma |F_o^2 - F_o^2(\text{mean})|/\Sigma[F_o^2]$ calculated only for data of crystal N.2.
‖ NP = number of refine parameters.

TABLE 3. Fractional coordinates and displacement parameters obtained with the data from crystals BTS-308 N.2 and N.3

P (GPa)		0.0001	0.047	0.984	1.794	3.167	3.172*	3.587	3.649	6.409*	7.762	9.405
M1	x	0.2505(4)	0.2514(4)	0.2520(4)	0.2513(4)	0.2509(3)	0.2505(4)	0	0	0	0	0
	y	0.6546(2)	0.6549(3)	0.6560(3)	0.6559(3)	0.6565(2)	0.6563(3)	0.9063(3)	0.9064(3)	0.9072(3)	0.9077(3)	0.9080(4)
	z	0.2322(5)	0.2331(5)	0.2328(6)	0.2305(5)	0.2286(4)	0.2284(4)	0.25	0.25	0.25	0.25	0.25
	U_eq	0.0104(9)	0.0113(7)	0.0115(7)	0.0108(7)	0.0103(6)	0.0100(6)	0.0096(7)	0.0098(8)	0.0108(8)	0.0113(9)	0.011(1)
M2	x	0.2558(5)	0.2564(5)	0.2559(5)	0.2564(5)	0.2573(4)	0.2562(5)	0	0	0	0	0
	y	0.0177(4)	0.0188(4)	0.0206(4)	0.0205(4)	0.0219(4)	0.0218(4)	0.2775 (2)	0.2779(2)	0.2792(2)	0.2797(2)	0.2805(3)
	z	0.2294(6)	0.2300(5)	0.2280(5)	0.2272(5)	0.2245(6)	0.2234(4)	0.25	0.25	0.25	0.25	0.25
	U_eq	0.0135(7)	0.0142(6)	0.0140(6)	0.0134(7)	0.0120(6)	0.0111(6)	0.0150(7)	0.0157(8)	0.0146(7)	0.0148(8)	0.014(1)
M21	x	0.246(7)	0.252(7)	0.248(7)	0.250(7)	0.238(5)	0.251(7)	0	0	0	0	0
	y	0.039(5)	0.027(6)	0.016(6)	0.033(6)	0.033(6)	0.028(5)	0.2775(2)	0.2779(2)	0.2792(2)	0.2797(2)	0.2805(3)
	z	0.264(9)	0.283(7)	0.281(8)	0.279(7)	0.256(9)	0.277(6)	0.25	0.25	0.25	0.25	0.25
	U_iso	0.03†	0.03†	0.03†	0.03†	0.03†	0.03†	0.0150(7)	0.0157(8)	0.0146(7)	0.0148(8)	0.014(1)
TA	x	0.0428(5)	0.0432(4)	0.0428(4)	0.0426(5)	0.0412(4)	0.0418(4)	0.2957(3)	0.2956(3)	0.2957(3)	0.2959(3)	0.2954(4)
	y	0.3400(3)	0.3401(4)	0.3411(4)	0.3416(4)	0.3417(3)	0.3417(3)	0.0905(2)	0.0905(2)	0.0912(2)	0.0911(2)	0.0911(3)
	z	0.2745(5)	0.2748(6)	0.2747(6)	0.2736(6)	0.2732(5)	0.2740(5)	0.2240(3)	0.2237(4)	0.2207(4)	0.2203(4)	0.2188(5)
	U_iso	0.0086(6)	0.0100(7)	0.0106(7)	0.0097(7)	0.0099(6)	0.0086(6)	0.0075(6)	0.0081(7)	0.0084(6)	0.0090(8)	0.0083(9)
TB	x	0.5482(5)	0.5477(4)	0.5489(4)	0.5492(4)	0.5499(4)	0.5497(4)					
	y	0.8383(3)	0.8377(4)	0.8370(4)	0.8382(4)	0.8378(3)	0.8380(3)					
	z	0.2384(5)	0.2385(5)	0.2375(5)	0.2360(5)	0.2332(4)	0.2334(5)					
	U_iso	0.0089(6)	0.0083(6)	0.0088(7)	0.0085(7)	0.0071(6)	0.0079(6)					
O1A	x	0.867(1)	0.869(1)	0.870(1)	0.868(1)	0.8676(9)	0.8668(9)	0.1221(7)	0.1216(8)	0.1209(8)	0.1218(9)	0.1217(9)
	y	0.3374(7)	0.3378(9)	0.3409(9)	0.3380(8)	0.3400(7)	0.3381(7)	0.0895(5)	0.0893(6)	0.0891(6)	0.0889(6)	0.0890(7)
	z	0.168(1)	0.170(1)	0.170(1)	0.169(1)	0.171(1)	0.171(1)	0.1431(9)	0.143(1)	0.141(1)	0.142(1)	0.139(1)
	U_iso	0.008(1)	0.012(2)	0.010(2)	0.009(2)	0.010(1)	0.008(1)	0.010(1)	0.001(1)	0.009(1)	0.008(1)	0.007 (1)
O1B	x	0.373(1)	0.371(1)	0.372(1)	0.373 (1)	0.3742(8)	0.3741(9)					
	y	0.8373(7)	0.8379(8)	0.8375(9)	0.8385(9)	0.8378(7)	0.8374(7)					
	z	0.133 (1)	0.133(1)	0.132(1)	0.133(1)	0.131(1)	0.131(1)					
	U_iso	0.009(1)	0.009(2)	0.010 (2)	0.010 (2)	0.009(1)	0.008(1)					
O2A	x	0.118 (1)	0.123(1)	0.123(1)	0.123(1)	0.1200(8)	0.1187(9)	0.3741(7)	0.3732(8)	0.3738(8)	0.3739(8)	0.3732(9)
	y	0.4971(8)	0.4987(8)	0.4999(9)	0.5002(9)	0.5035(7)	0.5021(8)	0.2400(6)	0.2395(7)	0.2408(7)	0.2411(7)	0.2428(8)
	z	0.330(1)	0.333(1)	0.333(1)	0.333(1)	0.330(1)	0.329(1)	0.3598(9)	0.360(1)	0.359(1)	0.360(1)	0.361(1)
	U_iso	0.012(2)	0.011(2)	0.009(2)	0.013(2)	0.009(1)	0.012(1)	0.012(1)	0.012(1)	0.012(1)	0.013(1)	0.010(2)
O2B	x	0.633(1)	0.628(1)	0.627(1)	0.627(1)	0.6259(9)	0.628(1)					
	y	0.9886(8)	0.9868(9)	0.989(1)	0.9894(9)	0.9876(7)	0.9878(7)					
	z	0.372(1)	0.367(2)	0.368(2)	0.370(1)	0.370(1)	0.371(1)					
	U_iso	0.017(2)	0.020(2)	0.019(2)	0.015(2)	0.015(1)	0.013(1)					
O3A	x	0.100(1)	0.104(1)	0.105(1)	0.102(1)	0.104(1)	0.103(1)	0.3521(7)	0.3517(8)	0.3527(8)	0.3517(8)	0.352(1)
	y	0.2599(8)	0.2621(9)	0.260(1)	0.260(1)	0.2623(8)	0.2616(8)	0.0485(6)	0.0496(7)	0.0509(7)	0.0523(7)	0.0523(8)
	z	0.572(2)	0.574(2)	0.576(2)	0.572(2)	0.573(1)	0.575(1)	0.948(1)	0.945(1)	0.939(1)	0.936(1)	0.935(1)
	U_iso	0.020(2)	0.020(2)	0.021(2)	0.024(2)	0.022(2)	0.020(2)	0.015(1)	0.015(1)	0.015(1)	0.015(2)	0.013(2)
O3B	x	0.607(1)	0.606(1)	0.606(1)	0.605(1)	0.6070(9)	0.607(1)					
	y	0.7130(8)	0.7128(9)	0.711(1)	0.709(1)	0.7059(7)	0.7055(8)					
	z	0.484(1)	0.484(2)	0.478(2)	0.475(2)	0.470(1)	0.471(1)					
	U_iso	0.016(2)	0.018(2)	0.017(2)	0.020(2)	0.015(2)	0.013(2)					

Notes: Estimated pressures errors 0.05 GPa.
* Data measured during decompression. For all high-pressure data, the Mg and Fe site occupancies of the M1 and M2 sites were constrained to those obtained for crystal N.2 for which the structure refinement was performed using the data collected with crystal in air. M1 = Fe₀.₂₅₃, Mg₀.₇₄₇; M2 = Fe₀.₇₅₅, Mg₀.₁₂₄, Ca₀.₁₂₁.
† These thermal parameters were not refined for the high-pressure crystal structure and were fixed to the value observed with the crystal measured in air.

TABLE 4a. Selected bond lengths (Å) and angles (°) in $P2_1/c$ structures refined with the data from crystals BTS-308 N.2 and N.3 (atom nomenclature as in Burnham et al. 1967)

P (GPa)	0.0001	0.047	0.984	1.794	3.167	3.172*
TA-O1A	1.627(9)	1.610(8)	1.593(8)	1.605(8)	1.609(5)	1.603(8)
TA-O2A	1.569(8)	1.597(8)	1.595(8)	1.590(9)	1.588(5)	1.587(7)
TA-O3A	1.645(8)	1.647(9)	1.662(9)	1.654(9)	1.647(5)	1.647(7)
TA-O3A	1.620(9)	1.637(9)	1.626(9)	1.619(10)	1.633(5)	1.621(8)
<TA-O>	1.615(4)	1.623(4)	1.619(4)	1.617(5)	1.619(3)	1.615(4)
V_{TA} (Å³)	2.14(1)	2.17(1)	2.16(1)	2.15(1)	2.165(7)	2.14(2)
TQE_{TA}	1.0063	1.0079	1.0073	1.0079	1.0078	1.0073
TAV_{TA}	24.82	32.32	30.78	33.11	31.78	29.87
TB-O1B	1.617(9)	1.625(8)	1.629(8)	1.614(9)	1.605(5)	1.608(8)
TB-O2B	1.617(8)	1.583(9)	1.595(9)	1.590(9)	1.585(5)	1.581(7)
TB-O3B	1.666(8)	1.664(9)	1.642(9)	1.656(9)	1.653(5)	1.668(7)
TB-O3B	1.673(8)	1.667(9)	1.672(9)	1.666(9)	1.667(5)	1.657(7)
<TB-O>	1.643(4)	1.635(4)	1.634(4)	1.631(4)	1.628(3)	1.629(4)
V_{TB} (Å³)	2.25(1)	2.23(1)	2.23(1)	2.22(1)	2.199(6)	2.20(2)
TQE_{TB}	1.0072	1.0055	1.0043	1.0041	1.0045	1.0043
TAV_{TB}	30.06	21.40	16.63	16.31	17.57	16.89
TILT B (°)	4.7(1)	5.1(1)	4.6(1)	5.2(1)	4.0(1)	4.0(1)
TILT A (°)	6.3(1)	5.2(1)	5.2(1)	5.3(1)	5.2(1)	5.0(2)
O3B-O3B-O3B (°)	151.7(6)	151.5(7)	150.4(7)	148.9(7)	146.9(4)	146.7(5)
O3A-O3A-O3A (°)	187.7(6)	189.4(7)	187.4(8)	187.6(8)	189.4(4)	189.6(6)
ΔO3-O3-O3 (°)	36.1(7)	38(1)	37(1)	39(1)	42.5(3)	43.7(6)
M1-O1A	2.151(8)	2.162(8)	2.176(8)	2.142(8)	2.132(5)	2.122(7)
M1-O1A	2.050(7)	2.065(7)	2.063(7)	2.046(7)	2.030(4)	2.032(6)
M1-O1B	2.183(8)	2.170(8)	2.150(8)	2.158(8)	2.145(5)	2.149(7)
M1-O1B	2.066(7)	2.051(7)	2.043(7)	2.064(7)	2.073(4)	2.058(6)
M1-O2A	2.080(8)	2.052(8)	2.043(8)	2.037(9)	2.028(5)	2.039(7)
M1-O2B	2.044(8)	2.076(9)	2.058(9)	2.053(9)	2.049(5)	2.059(7)
<M1-O>	2.095(3)	2.096(3)	2.089(3)	2.083(3)	2.076(2)	2.076(3)
V_{M1} (Å³)	12.15(3)	12.15(3)	12.05(3)	11.95(3)	11.83(2)	11.84(3)
OQE_{M1}	1.0074	1.0074	1.0065	1.0064	1.0057	1.0060
OAV_{M1}	22.48	22.57	19.10	19.79	17.65	18.56
M2-O1A	2.172(8)	2.187(9)	2.176(9)	2.182(8)	2.164(5)	2.179(7)
M2-O1B	2.129(8)	2.119(8)	2.129(9)	2.116(9)	2.116(5)	2.127(7)
M2-O2A	2.103(7)	2.081(7)	2.068(7)	2.071(7)	2.088(4)	2.074(6)
M2-O2B	2.027(8)	2.056(8)	2.060(8)	2.057(8)	2.055(5)	2.057(6)
M2-O3A$_S$	2.477(9)	2.438(9)	2.420(10)	2.434(10)	2.393(6)	2.396(8)
M2-O3A$_L$	3.454(9)	3.450(9)	3.409(9)	3.411(10)	3.407(7)	3.413(8)
M2-O3B$_S$	2.655(9)	2.650(9)	2.596(10)	2.568(10)	2.492(5)	2.497(8)
M2-O3B$_L$	2.928(9)	2.920(10)	2.924(10)	2.947(10)	2.955(8)	2.966(8)
<M2-O>	2.261(3)	2.255(3)	2.241(3)	2.238(3)	2.218(2)	2.222(3)
V_{M2} (Å³)	13.88(3)	13.80(3)	13.61(3)	13.52(3)	13.23(2)	13.30(4)
OQE_{M2}	1.0827	1.0805	1.0763	1.0769	1.0713	1.0714
OAV_{M2}	227.71	223.72	217.86	220.28	212.45	211.39

Note: Estimated pressures errors 0.05 GPa; S and L subscripts refer to the short and long distances, respectively; TQE, TAV, OQE, and OAV are quadratic elongation and angle variance for tetrahedra and octahedra (Robinson et al. 1971); polyhedral volumes calculated with IVTON (Balić-Žunić and Vicković 1996).
* Data measured during decompression.

TABLE 4b. Selected bond lengths (Å) and angles (°) in $C2/c$ structures refined with the data from crystals BTS-308 N.2 and N.3 (atom nomenclature as in Burnham et al. 1967)

P (GPa)	3.587	3.649	6.409*	7.762	9.405
T-O1	1.603(6)	1.602(7)	1.604(7)	1.593(7)	1.585(8)
T-O2	1.585(5)	1.580(6)	1.581(6)	1.581(7)	1.592(7)
T-O3	1.655(5)	1.666(6)	1.660(6)	1.659(6)	1.650(7)
T-O3	1.665(5)	1.664(6)	1.662(6)	1.655(6)	1.651(7)
<T-O>	1.627(11)	1.628(13)	1.627(12)	1.622(13)	1.620(15)
V_T (Å³)	2.198(7)	2.203(9)	2.197(8)	2.178(9)	2.168(10)
TQE	1.0041	1.0039	1.0043	1.0042	1.0041
TAV	17.64	16.23	18.43	17.92	17.61
TILT (°)	5.14(8)	5.13(8)	4.88(10)	5.05(8)	4.49(17)
O3-O3-O3 (°)	142.4(4)	141.8(5)	140.9(5)	140.2(5)	138.9(8)
M1-O1 ×2	2.132(5)	2.129(5)	2.101(6)	2.093(6)	2.087(7)
M1-O1 ×2	2.045(5)	2.041(5)	2.028(5)	2.028(6)	2.012(7)
M1-O2 ×2	2.052(6)	2.061(7)	2.034(6)	2.029(7)	2.018(7)
<M1-O>	2.076(13)	2.077(14)	2.054(14)	2.050(15)	2.039(17)
V_{M1} (Å³)	11.87(2)	11.87(2)	11.49(2)	11.43(2)	11.25(2)
OQE_{M1}	1.0042	1.0046	1.0043	1.0037	1.0034
OAV_{M1}	13.02	14.11	13.54	11.93	10.36
M2-O1 ×2	2.165(5)	2.167(6)	2.156(6)	2.157(6)	2.157(7)
M2-O2 ×2	2.051(5)	2.054(5)	2.051(5)	2.043(6)	2.037(7)
M2-O3 ×2	2.451(5)	2.438(6)	2.377(6)	2.355(6)	2.337(7)
<M2-O>	2.222(12)	2.220(14)	2.195(14)	2.185(15)	2.177(17)
V_{M2} (Å³)	14.25(2)	14.21(2)	13.75(2)	13.57(2)	13.42(3)
OQE_{M2}	1.0236	1.0227	1.0205	1.0199	1.0198
OAV_{M2}	51.90	51.11	51.39	50.52	51.22
M2-O3$_L$ ×2	2.994(6)	3.009(7)	2.999(7)	3.008(7)	2.994(9)

Note: Estimated pressures errors 0.05 GPa; M2-O3$_L$ are the longest M2-O3 distances; TQE, TAV, OQE, and OAV are quadratic elongation and angle variance for tetrahedra and octahedra (Robinson et al. 1971); polyhedral volumes calculated with IVTON (Balić-Žunić and Vicković 1996).
* Data measured during decompression.

Hugh-Jones and Angel 1994), at *P* between 5.0 and 7.0 GPa, and for a synthetic, Ca-rich, and iron-free pigeonite, $Ca_{0.15}Mg_{1.85}Si_2O_6$ (Nestola et al. 2004), at *P* = 5.1 GPa.

The volume-pressure data for both low- and high-symmetry phases were fitted by third-order (BM3-EoS) and second-order (BM2-EoS) Birch-Murnaghan equations of state, respectively (Birch 1947), using the EOSFIT-5.2 software (Angel 2002). The fit provided the EoS coefficients reported in Table 5. The bulk modulus and first derivative values are in excellent agreement with the values obtained from the normalized stress F_E-eulerian strain f_E plot (Angel 2000a). The $C2/c$ phase has a bulk modulus (K_{T0}) that is 13.5% larger than that obtained for the $P2_1/c$ phase, indicating a significantly higher stiffness.

The axial moduli for *a*, *b*, *c*, and *a*sinβ for the $P2_1/c$ and $C2/c$ phases of our sample were obtained using a parameterized form of the BM3-EoS and BM2-EoS, respectively, in which the

individual axes are cubed, following the procedure implemented in the EoS-FIT5.2 program (Angel 2002). The results obtained are reported in Table 5. In general the compression of a crystal due to hydrostatic pressure varies with direction. The relationship between stress (applied pressure) and strain (deformation of the crystal) can be expressed in terms of the linear compressibility of the crystal as: $\beta = \Sigma_{i,k=1,2,3} s_{ij} l_i l_j$ (in Voigt notation) where *l* is the unit vector direction and s_{ij} represents the fourth-rank elastic tensor. The incremental Lagrangian finite strain tensor component can be derived from the unit-cell parameters measured at different pressures (Schlenker et al. 1978) and these can be equated to the sums of the compliance tensor components with the assumption that experimental strain increments and pressure interval are small (Brown et al. 2006). The compliance tensor sums were calculated from the unit-cell parameter variation with pressure using the WinStrain program, a modified version of the Strain program by Ohashi (1972), kindly provided by R.J. Angel (Virginia Tech), according to the orthogonal basis set with the *y* axis aligned parallel to the *b* axis of the crystal, the *z* axis along the *c** direction, and the *x* axis parallel to the *a* axis. The results are plotted vs. the incremental pressure midpoints in Figure 2. There is some scatter of the data at pressures close to P_c, but in the stability field of the $P2_1/c$ and HP $C2/c$ phases the compliance tensor sums vary linearly with pressure and therefore can be extrapolated to 1 bar using linear fits (Table 5). Since the axial K_{T0} parameter refined in a linearized EoS is one-third of the inverse of the compressibility [$K_{T0} = -1/(3\beta_0)$] (Angel 2000a), it is possible to compare directly this quantity with the appropriate zero value of the compliance tensor sums, taking into account the orthogonal coordinate system used. In this case $K_{T0}(a)$ and $K_{T0}(b)$ can be compared with the compliance tensor sums ($s_{11}+s_{12}+s_{13}$),
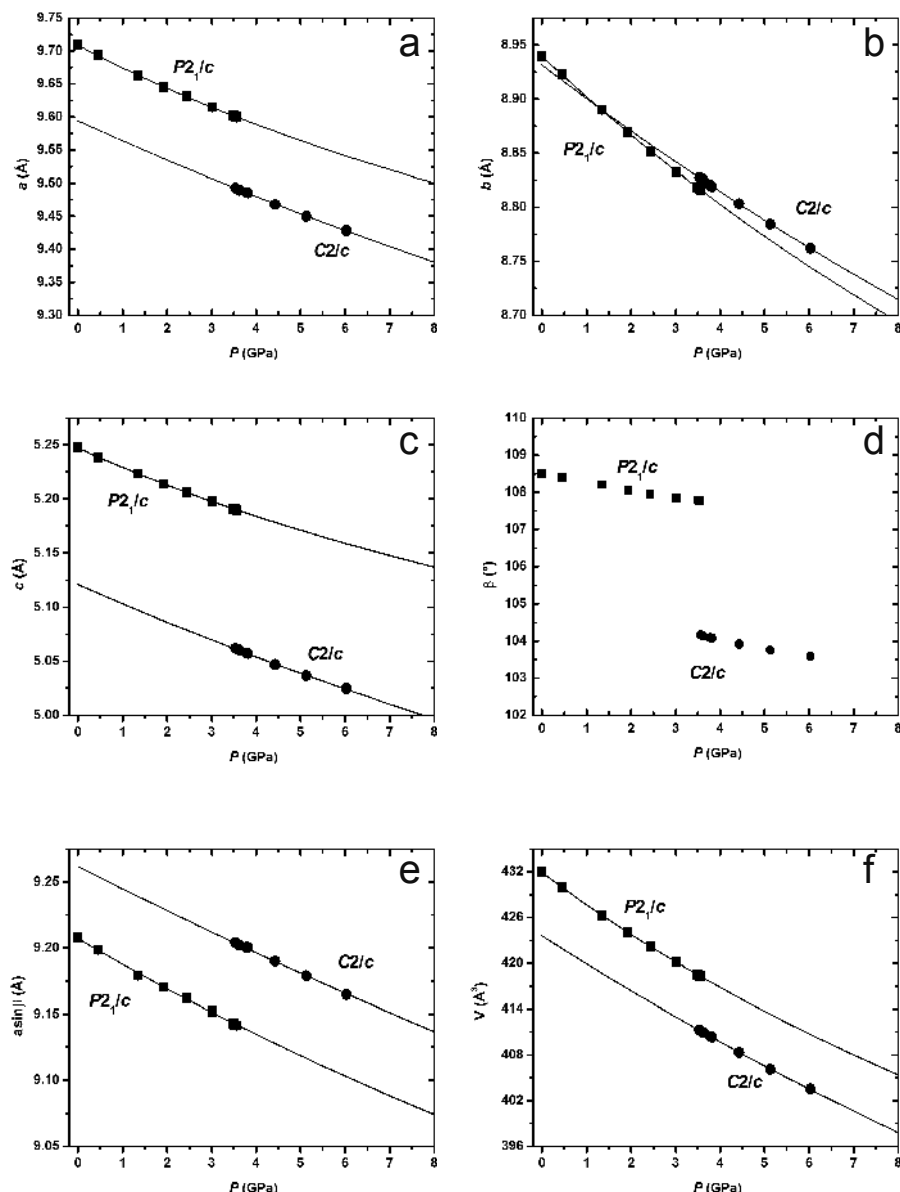
FIGURE 1. Unit-cell parameter as a function of pressure, P, for the BTS-308 sample. The $P2_1/c$ data were fitted using a third-order Birch-Murnaghan equation of state; the $C2/c$ data were fitted using a second-order Birch-Murnaghan equation of state (see text). The uncertainties in the measurements are considerably smaller than the size of the symbols used.

and ($s_{21}+s_{22}+s_{23}$), respectively. Moreover, since the z axis of the orthogonal system lies along c^*, we can compare ($s_{31}+s_{32}+s_{33}$) with the "linearized"-K_{T0} value of the $c\sin\beta$ direction. There is a good agreement (between 2 and 3.5%) between the two sets of data of the HP $C2/c$, and this indicates that the BM2-EoS fits of the HP $C2/c$ data properly describe the high-pressure behavior of the high-pressure phase, at least in the investigated pressure range. For the $P2_1/c$ phase, the agreement is excellent for the $c\sin\beta$ direction, but is on the order of 15–20% for the a and b directions. However for these two directions both sets of data show the same compressibility scheme with the b axis more compressible than the a axis.

From the linear axial compressibilities reported in Table 5

the following compressibility schemes can be calculated: $\beta_b >> \beta_a \geq \beta_c >> \beta_{a\sin\beta} \approx \beta_{c\sin\beta}$ (2.05:1.74:1.70:1.02:1.00) and $\beta_b \approx \beta_c > \beta_a >> \beta_{c\sin\beta} > \beta_{a\sin\beta}$ (1.83:1.81:1.66:1.12:1.00) for the $P2_1/c$ and the $C2/c$ phases, respectively. The axial anisotropy is smaller for the higher symmetry phase, whereas the $a\sin\beta$ and $c\sin\beta$ directions are the stiffest in both phases (Nestola et al. 2004 and references therein).

The data on the BTS-308 pigeonite can be used to quantify the common effect of Ca and Fe substitution into the clinoenstatite structure. Consequently, the transition pressure, P_c, measured in this study has been plotted against average ionic radius of the cation at the M2 site (Fig. 3) and compared with the data available in the literature for the $MgSiO_3$-$FeSiO_3$ join,

TABLE 5. Fitted unit-cell parameters, bulk moduli, and first derivative of the bulk modulus at room pressure of the $P2_1/c$ and $C2/c$ phases obtained using a BM3 and BM2 EoS, respectively

	$P2_1/c$						$C2/c$					
	a (Å)	b (Å)	c (Å)	$a\sin\beta$ (Å)	$c\sin\beta$ (Å)	V (Å³)	a (Å)	b (Å)	c (Å)	$a\sin\beta$ (Å)	$c\sin\beta$ (Å)	V (Å³)
Y_0	9.7087(2)	8.940(3)	5.247(1)	9.208(4)	4.9766(2)	431.934(17)	9.594(2)	8.9315(8)	5.120(1)	9.264(1)	4.9441(5)	423.6(1)
K_0	89(1)	75.4(1.1)	90.3(1.2)	151.7(5.9)	154.5(5.8)	96.8(8)	103(2)	93.6(7)	94(2)	175(3)	152.3(1.7)	112.4(8)
K'	10(1)	5.8(7)	10.8(8)	7.7(3.7)	9.9(3.7)	8.5(5)	4	4	4	4	4	4
$1/3\times(1/K_0)$ calculated	0.00376	0.00442			0.00216		0.00322	0.00356			0.00219	
$1/3\times(1/K_0)$ fitted*	0.00321	0.00355			0.00214		0.00314	0.00344			0.00215	
m ($\times10^{-6}$)†	4.46	4.79			4.46		7.74	8.70			14.00	

Note: The first pressure derivative (K') was constrained to 4 for the $C2/c$ phase.
* Intercept at room pressure of the compliance components sums obtained through linear fitting (y = mx + b).
† m = slope of the linear fitting of the compliance components sums.
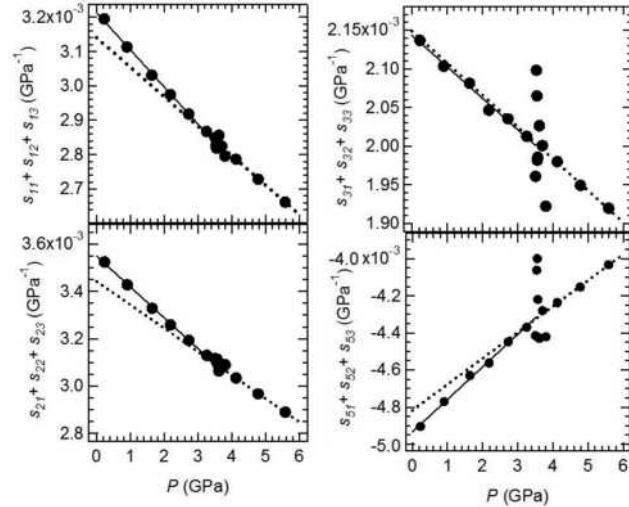
FIGURE 2. Compliance tensor sums calculated from the incremental of the unit-cell parameters plotted against the mean pressure of each increment. The solid line is the linear fit through the $P2_1/c$ data, whereas the dotted line is the linear fit through the HP $C2/c$ data.

FIGURE 3. Average cation size of the M2 site vs. transition pressure P_c for different clinopyroxenes. The solid line is the linear fit through the FeMg-cpx data (1 = En_{100}; 2 = $En_{80}Fs_{20}$; 3 = $En_{70}Fs_{30}$; 4 = $En_{60}Fs_{40}$; 5 = $En_{40}Fs_{60}$; 6 = $En_{20}Fs_{80}$; 7 = Fs_{100}); the dashed line is the linear fit through the data of samples with larger cations in M2 site. The BTS-308 pigeonite sample (P_c = 3.57 GPa) follows the dashed line trend, along with the two Mn-pyroxenes and the other Ca-rich pyroxene (Di15En85). The CrMg-pyroxene lies in between the two trends.

the $MnSiO_3$-$MgSiO_3$ join, $CrMgSi_2O_6$, and $CaMgSi_2O_6$ samples (Angel et al. 1992; Hugh-Jones et al. 1994; Ross and Reynard 1999; Arlt et al. 1998; and Nestola et al. 2004, respectively). As observed by Arlt et al. (1998), two different trends are visible: (1) defined by the Fe,Mg-clinopyroxenes, and (2) defined by the samples with larger divalent cation at M2 site, whereas the $CrMgSi_2O_6$ sample appears to lie between the two trends. Arlt et al. (1998) suggested that these two trends are due to crystal field energy (CFE), which stabilizes Fe (and Cr in a minor extent) in the smaller octahedra of the HP $C2/c$ structure with respect to the $P2_1/c$ structure. If this suggestion is correct, the fact that the BTS-308 sample lies on the trend defined by the larger cations and not on the trend defined by the Fe,Mg-pyroxenes indicates that size rather than CFE is primarily responsible for the decrease of the transition pressure.

Polyhedral compressibility and distortion parameters

The evolution of the M2 and M1 polyhedral volumes as a function of pressure is shown in Figures 4a and 4b. To better understand the mechanism of the $P2_1/c$-$C2/c$ phase transition, the M2 polyhedral volume has been calculated considering the cation at the M2 site coordinated by 8 O atoms. At the transition pressure, the volumes of the M1 and M2 polyhedra show a significant discontinuity corresponding to a slight volume increase (0.34%) for the M1 polyhedron and to an abrupt decrease (2.4%)

for the M2 polyhedron. The values of linear volume compressibilities of the M1 and M2 polyhedra (β_{M1} and β_{M2}) are reported in Table 6 for both $P2_1/c$ and HP $C2/c$ phases. For the BTS-308 pigeonite sample we observe that: (1) the M2 polyhedron is more compressible than the M1 polyhedron in the $P2_1/c$ phase; (2) the M2 polyhedron is less compressible than the M1 polyhedron in the HP $C2/c$ phase; and (3) the M2 polyhedron of the $P2_1/c$ phase is strongly more compressible than the M2 polyhedron of the HP $C2/c$ phase, whereas there is no significant difference between the M1 polyhedra of the two phases. It appears, therefore, that the larger compressibility of the $P2_1/c$ phase with respect to that of the HP $C2/c$ is due to the distortion of the M2 polyhedra. In contrast, the M2 site of $C2/c$ hedenbergite (Nestola et al. 2008b) and diopside (Thompson and Downs 2008) is slightly more compressible than the M1 site (Table 6). This may be due to the fact that, in these end-member pyroxenes, the M2 site is fully occupied by Ca and therefore more compressible than the pigeonite M2 site, which is partially occupied by small Mg/Fe cations, as well as to the fact that the bonding topology of the M2 site in the HT $C2/c$ phases (hedenbergite and diopside)
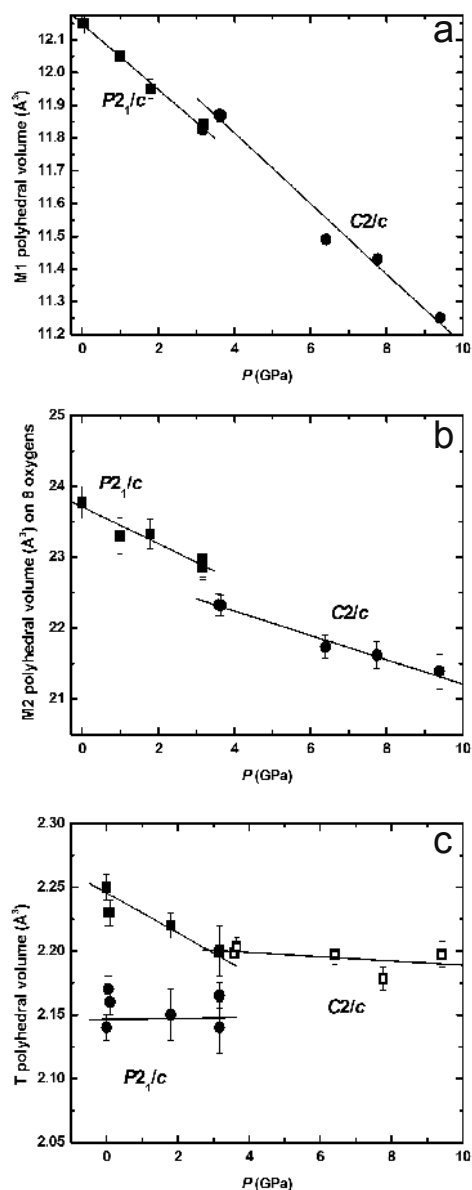
FIGURE 4. Variation of the polyhedral volumes with pressure for $P2_1/c$ and $C2/c$ phases: (**a**) M1 polyhedra, (**b**) M2 polyhedra, and (**c**) T polyhedra.

TABLE 6. Elastic properties of polyhedra in clinopyroxenes

Samples	$P2_1/c$ β_{M1} (GPa^{-1})	$C2/c$ β_{M1} (GPa^{-1})	$P2_1/c$ β_{M2} (GPa^{-1})	$C2/c$ β_{M2} (GPa^{-1})	Ref.
$CaFeSi_2O_6$*	–	6.7×10^{-3}	–	8.46×10^{-3}	Zhang et al. (1997)
$CaFeSi_2O_6$*	–	8.6×10^{-3}	–	9.2×10^{-3}	Nestola et al. (2008b)
$Ca_{0.19}Mg_{0.95}Fe_{0.85}Si_2O_6$	8.02×10^{-3}	8.92×10^{-3}	12.12×10^{-3}	7.23×10^{-3}	our sample
$Ca_{0.15}Mg_{1.85}Si_2O_6$	10.47×10^{-3}	–	10.22×10^{-3}	–	Nestola et al. (2004)
$CaMgSi_2O_6$*	–	7.74×10^{-3}	–	8.02×10^{-3}	Thompson and Downs (2008)

* HT topology.

polyhedron remains practically unchanged until the transition pressure ($\beta_{TA} = 0.7 \times 10^{-3}$ GPa^{-1}), however, the TB polyhedron exhibits a significant decrease in volume of about 2.2% ($\beta_{TB} = 7.0 \times 10^{-3}$ GPa^{-1}) (Fig. 4c) and becomes more regular as indicated by the decrease in tetrahedral angle variance (TAV, Robinson et al. 1971) and in tetrahedral quadratic elongation (TQE, Robinson et al. 1971) (Table 4a). After the phase transition, from 3.58 to 9.40 GPa, the T polyhedron of the HP $C2/c$ phase shows just a very slight decrease in volume ($\beta_T = 2.4 \times 10^{-3}$ GPa^{-1}).

Kinking angles

Figure 5a reports the evolution of the O3-O3-O3 kinking angle with pressure and temperature far from the transition point. In the $P2_1/c$ phase, the A chain is S-rotated, whereas the B chain is O-rotated, in the sense of Thompson (1970), and thus the shrinking along [001] in both chains occurs in the opposite sense. For our sample in the $P2_1/c$ phase, the O3A-O3A-O3A angle, expressed as 360-(O3A-O3A-O3A), increases by 1.9° (Table 4) and O3B-O3B-O3B angle decreases by nearly 5°. At the transition, the two tetrahedral chains become equivalent and O-rotated with a kinking angle that is smaller than those of the $P2_1/c$ structure. In the HP $C2/c$ phase, the kinking angle decreases following a non-linear trend by about 3.5° from 3.58 to 9.38 GPa, thus resulting in a stiffer behavior compared to that expected considering the average deformation of both the A and B chains in the $P2_1/c$ phase. The behavior of the kinking angle of the A and B chains with increasing pressure is compared with that observed for the same sample with increasing temperature (Cámara et al. 2002) in Figure 5a. It is evident that for the sample of this study the transition at high temperature occurs with a progressive change in rotation of both A and B chains that become more elongated with increasing temperature, as expected for the second-order character of the HT transition, which occurs at 758 °C for a natural sample of BTS-308 (Cámara et al. 2003a), whereas the transition at HP occurs with an abrupt change in the sense of rotation of the A chain (Hugh-Jones et al. 1994; Nestola et al. 2004).

Bond lengths

In the stability field of the $P2_1/c$ phase, the main deformation between room pressure and 3.17 GPa occurs at a direction oriented at about 45° with respect to the *b* axis on the equatorial plane of the octahedron. Such direction is represented by the two M1-O2A and M1-O1B distances, which show a contraction of 2.5 and 1.7%, respectively (Table 4a). The other four individual M1-O bond lengths do not show any significant variation larger

may be different from that in the HP $C2/c$ and in $P2_1/c$ phases. There are no compressibility data relative to the HP $C2/c$ phase of the synthetic $Ca_{0.15}Mg_{1.85}Si_2O_6$ sample studied by Nestola et al. (2004); however, for this sample the M1 and M2 sites of the $P2_1/c$ phase have similar compressibility. The large difference in compressibility between the M1 and M2 sites of the $P2_1/c$ natural pigeonite studied in this work appears, therefore, related to the combined presence of Ca and Fe at the M2 site. Both M1 and M2 octahedra become more regular in the HP $C2/c$ phase as shown by the decrease in mean quadratic elongation (OQE, Robinson et al. 1971) and in octahedral angle variance (OAV, Robinson et al. 1971) (Table 4).

For most silicates the Si tetrahedra are considered as rigid units, i.e., practically not compressible up to 7–10 GPa (Zhang et al. 1997). Indeed, within the $P2_1/c$ stability field, the TA

than 1%. Within the stability field of the HP $C2/c$ phase the three pairs of independent bond lengths of the M1 site all show a contraction of about 2% in the pressure region between 3.6 and 9.4 GPa.

Among the individual M2-O bond lengths, the four M2-O3 distances, including the longest that are out of coordination in both phases, are the most affected by pressure. In particular, as already shown by Nestola et al. (2004), at the transition pressure, the longest M2-O3A becomes equivalent to the shorter of the two M2-O3B. This behavior is clearly different from that occurring during the $P2_1/c$ to $C2/c$ high-temperature transition (see Cámara et al. 2002), where it is the longest M2-O3B that becomes equivalent to the shortest of the two M2-O3A (Fig. 5b). It is worth noting that at pressures lower than P_c, the variation of the two shorter M2-O3A and M2-O3B bond lengths is 3.3 and 6.3% respectively (see Table 4a), significantly larger than that of the two longer M2-O3 distances (~1%). At pressures above P_c, within the HP $C2/c$ stability field, the shortest M2-O3 distance decreases by 4.9%, whereas the longest one remains unchanged (Table 4b). The drawing reported in Figure 5c can help to understand the compression mechanism.

In a recent paper, McCarthy et al. (2008) suggested a possible application of "Bridgman's Law" to discuss the bonding topology of the M2-O3 bonds, which constitute the only significant topological difference among pyroxenes (Downs 2003). Bridgman (1923) found an empirical inverse relationship between the unit-cell volumes of isostructural materials at ambient conditions and their bulk moduli. The plot of bulk modulus vs. unit-cell volume data for several clinopyroxenes [Fig. 9 in McCarthy et al. (2008), in which the bulk moduli for all the available compositions were recalculated with a BM2] shows two clearly different trends, which have been attributed by the authors to the different bonding topology of the M2-O3 bonds. These bonds can be classified as "antipathetic" bonds (i.e., bonds whose decrease in length is inhibited by pressure-induced tetrahedral rotation, and therefore stiffen the structure) and "apathetic" bonds (those whose decrease in length is favored by tetrahedral rotation and therefore do not affect the host structure's stiffness). Two relationships have been thus suggested to predict the bulk modulus of any clinopyroxene knowing its bonding topology and its unit-cell volume at room conditions. These relationships are indeed valid for $LiGaSi_2O_6$, $Li(Al_{0.53}Ga_{0.47})Si_2O_6$ (Nestola et al. 2008c), and $NaTiSi_2O_6$ (Ullrich and Miletich 2008) for which the values of K_0 calculated according to the linear fits of McCarthy et al. (2008) agree within 3% for the Li compositions and 6% for the Na composition with the bulk modulus values obtained from fitting the P-V data with a second-order Birch-Murnhagan EoS. However, all pyroxenes considered by McCarthy et al. (2008) had either large monovalent or divalent cations (Na, Ca) or a small monovalent cation (Li) at the M2 site (with the exception of $ZnSiO_3$), while no Fe/Mg compositions have been taken into account. In Figure 6, we report, together with the data from McCarthy et al. (2008), the bulk moduli recalculated with a BM2 EoS for the following samples: BTS-308, i.e., a clinopyroxene with apathetic bonding topology in both low-P and high-P polymorphs; $P2_1/c$ clinoenstatite (Angel and Hugh-Jones 1994; Hugh-Jones and Angel 1994); clinoferrosilite (Hugh-Jones et al. 1994); and $P2_1/c$ Ca-rich clinoenstatite (Nestola et al. 2004).

These ferromagnesian clinopyroxenes clearly describe an intermediate trend with a slope practically parallel to the trend defined by the apathetic topologies but shifted up by ca. 20 GPa $[K_0 \text{ (GPa)} = -0.859V_0 \text{ (Å}^3) + 476, R^2 = 0.84]$. This difference may be due to compositional effects as well as to the fact that, at least for clinoenstatite and Ca-rich clinoenstatites, the values of K' are significantly larger than 4, in contrast with the samples considered by McCarthy et al. (2008), whose K' values are all close to 4. Note that the bulk moduli of HP $C2/c$ clinoenstatite
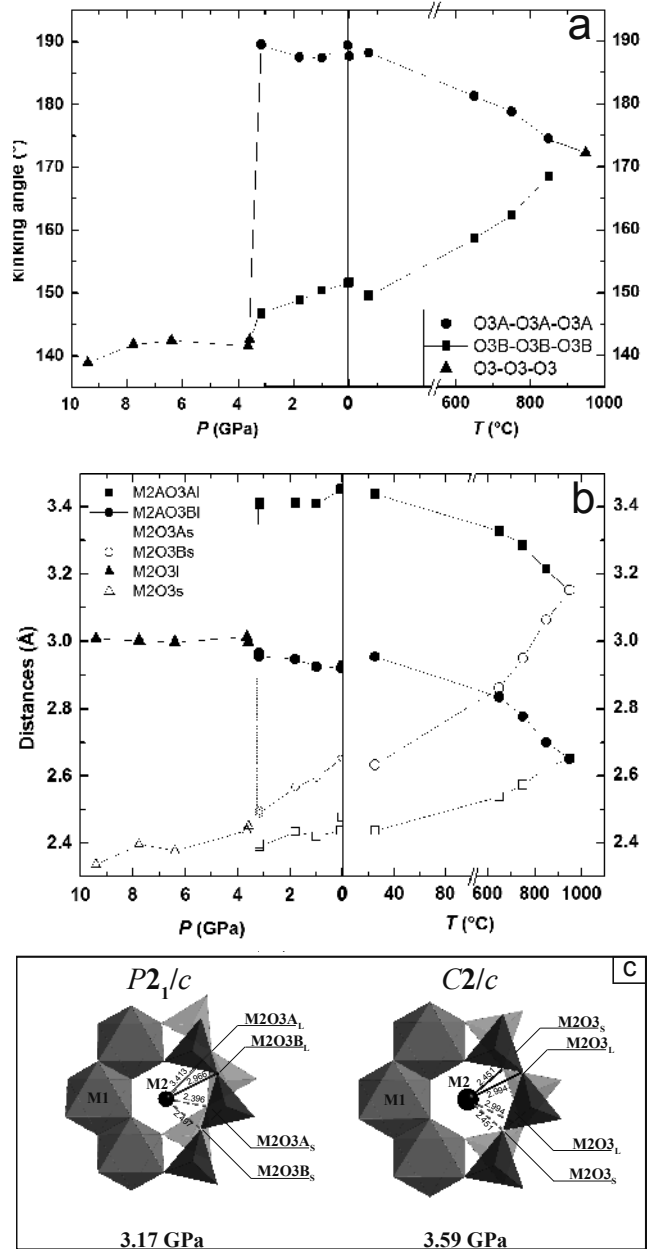

FIGURE 5. Variation with pressure and temperature for $P2_1/c$ and high-pressure and HT-$C2/c$ of (**a**) kinking angle and (**b**) M2-O3 distances. HT-$C2/c$ data are from Cámara et al. (2002). (**c**) Structure drawing showing changes in the M2 coordination geometry for the $P2_1/c$ structures at $P = 3.17$ GPa and for the $C2/c$ structure at $P = 3.59$ GPa. Distances between the M2 and O3 bridging O atoms are reported (in angstroms); the A chain is filled, the B chain open. The letters L and S stand for long and short bond distances.

(Angel and Hugh-Jones 1994; Hugh-Jones and Angel 1994) and $Di_{15}En_{85}$ (Nestola et al. 2004), for which only a limited range of pressure data were obtained, reducing the quality of BM2 fits, were not included in this new trend. If we use the linear fit of the ferromagnesian clinopyroxenes, we can predict a bulk modulus of 128 GPa for HP $C2/c$ clinoenstatite and 122 GPa for HP $C2/c$ $Di_{15}En_{85}$ composition.
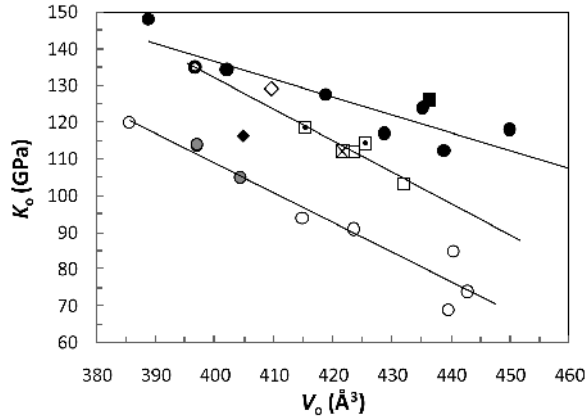

FIGURE 6. Bulk moduli recalculated with a BM2 EoS ($K' = 4$) vs. unit-cell volumes for $C2/c$ and $P2_1/c$ clinopyroxenes. Filled and open circles: data from Table 7 of McCarthy et al. (2008); filled square: $NaTiSi_2O_6$ [$V_0 = 436.35$ Å³, Ohashi et al. (1982); $K_0 = 126$ GPa, Ullrich and Miletich (2008)]; gray circles: $NaGaSi_2O_6$ [$P2_1/c$, $V_0 = 403.5(3)$ Å³, $K_0 = 105(2)$ GPa, Nestola et al. (2008c)] and $Li(Al_{0.53}Ga_{0.47})Si_2O_6$ [$P2_1/c$, $V_0 = 394.3(3)$ Å³, $K_0 = 114(2)$ GPa, Nestola et al. (2008c)]; black ring: $Li(Al_{0.53}Ga_{0.47})Si_2O_6$ [$C2/c$, $V_0 = 396.89(2)$ Å³, $K_0 = 135.2(9)$ GPa, Nestola et al. (2008c)]; crossed square: $Di_{15}En_{85}$ [$P2_1/c$, $V_0 = 421.68(4)$ Å³, $K_0 = 112(1)$ GPa, Nestola et al. (2004)]; dot centered open squares: $MgSiO_3$ [$P2_1/c$, $V_0 = 415.4(3)$ Å³, $K_0 = 119(1)$ GPa, Angel and Hugh-Jones (1994)], and $FeSiO_3$ [HP $C2/c$, $V_0 = 425.5(3)$ Å³, $K_0 = 114(7)$ GPa, Hugh-Jones et al. (1994)]; open squares: BTS-308 [$P2_1/c$, $V_0 = 431.9(2)$ Å³, $K_0 = 103(6)$ GPa] and BTS-308 [HP $C2/c$, $V_0 = 424(3)$ Å³, $K_0 = 112(1)$ GPa, this study]; filled diamond: $MgSiO_3$ [HP $C2/c$, $V_0 = 404.8(3)$ Å³, $K_0 = 116(5)$ GPa, Angel and Hugh-Jones (1994)]; $Di_{15}En_{85}$ [HP $C2/c$ $V_0 = 409.7(3)$ Å³, $K_0 = 129(2)$ GPa, Nestola et al. (2004)].

Spontaneous strain calculation

The spontaneous strain is a second-rank symmetric tensor that describes the lattice distortion associated with a phase transition (Salje 1991). The spontaneous strain components accompanying the $P2_1/c$ to HP $C2/c$ phase transition were calculated (Table 7) using the equations from Schlenker et al. (1978) as follows:

$$e_{11} = \frac{a}{a_0} - 1; \; e_{22} = \frac{b}{b_0} - 1; \; e_{33} = \frac{c \sin \beta}{c_0 \sin \beta_0} - 1 \tag{1}$$

$$e_{12} = 0; \; e_{13} = \left(\frac{c \cos \beta}{c_0 \sin \beta_0} - \frac{a \cos \beta_0}{a_0 \sin \beta_0} \right); e_{23} = 0.$$

The orientation for the Cartesian axis system is the same as that adopted by Carpenter et al. (1998) and reported above for the calculation of the compliance tensor. The reference parameters (a_0, b_0, c_0, β_0, and V_0) were obtained by extrapolation of the cell parameters of the HP $C2/c$ phase using the BM2 EoS parameters (Table 5) into the stability field of the low-pressure $P2_1/c$ phase (a, b, c, β, and V). The evolution of the angle β was obtained from the BM2-EoS fit of the HP $C2/c$ $c\sin\beta$ following a procedure similar to that described by Boffa Ballaran et al. (2000). Also the volume strain $V_s = (V - V_0)/V_0$, and the scalar strain, ε_s $\left(\varepsilon_s = \sqrt{\sum_{ij} e_{ij}^2} \right)$, were calculated (Table 7). Uncertainties for strain components, volume strain, and scalar strain (see Table 7) have been obtained by standard error propagation, through Equation 1, of the uncertainties in the low-P phase unit-cell parameters and the uncertainties in the extrapolated values of the high-P phase at $P < P_c$.

The strain component e_{22} is one order of magnitude smaller than the other strain components and therefore it can be considered negligible (see Table 7 and Fig. 7a). The strain components e_{33} and e_{13} increase with increasing P, whereas e_{11} decreases with increasing pressure (Figs. 7a and 7b). To check the reliability of the strain calculations we calculated the total strain ($e_{nsb} = \varepsilon_{11} + \varepsilon_{22} + \varepsilon_{33}$, where ε_{ii} are the eigenvalues of the diagonalized spontaneous strain tensor). For small strain $e_{nsb} = V_s$, and indeed

TABLE 7. Calculated strain components (e_{ij}), volume strain (V_s), scalar strain (ε_s), and total strain (e_{nsb}) and their e.s.d. values, at the different pressure values, obtained on the crystal BTS-308 N.1

P (GPa)	e_{11}	e_{22}	e_{33}	e_{13}	V_s	ε_s	e_{nsb}
0.00010(1)	0.01193(21)	0.00094(11)	0.00662(11)	−0.03202(59)	0.01958(26)	0.06549(115)	0.01949
0.458(4)*	0.01180(19)	0.00066(10)	0.00652(12)	−0.03223(53)	0.01908(25)	0.06586(103)	0.01898
1.348(5)*	0.01139(15)	0.00003(8)	0.00657(9)	−0.03280(40)	0.01805(19)	0.06690(79)	0.01799
1.929(7)	0.01132(12)	−0.00044(7)	0.00679(7)	−0.03283(33)	0.01770(16)	0.06697(64)	0.01766
2.437(5)	0.01143(10)	−0.00071(7)	0.00693(7)	−0.03316(26)	0.01768(14)	0.06765(51)	0.01766
3.014(5)	0.01139(7)	−0.00100(5)	0.00706(5)	−0.03354(19)	0.01749(11)	0.06842(38)	0.01745
3.496(5)*	0.01141(6)	−0.00117(5)	0.00702(5)	−0.03403(14)	0.01730(10)	0.06938(28)	0.01726
3.516(6)*	0.01137(7)	−0.00108(6)	0.00702(5)	−0.03405(14)	0.01734(10)	0.06941(28)	0.01731
3.551(5)	0.01144(6)	−0.00116(5)	0.00710(5)	−0.03410(14)	0.01740(10)	0.06952(27)	0.01738
3.567(5)	0.01141(6)	−0.00114(5)	0.00706(5)	−0.03411(14)	0.01736(10)	0.06954(27)	0.01733
3.536(6)*	0.00005(6)	0.00003(5)	0.00005(4)	−0.00023(14)	0.00011(10)	0.00047(28)	0.00013
3.603(6)	−0.00008(7)	0.00009(6)	0.00006(6)	−0.00021(13)	0.00006(11)	0.00045(26)	0.00007
3.627(7)*	−0.00006(7)	0.00004(6)	0.00004(5)	−0.00010(14)	−0.00002(11)	0.00022(25)	0.00002
3.780(6)*	−0.00001(5)	−0.00002(4)	−0.00003(3)	−0.00006(12)	−0.00007(8)	0.00013(23)	−0.00006
3.820(5)	0.00008(5)	−0.00003(4)	0.00003(3)	−0.00006(11)	0.00005(8)	0.00016(19)	0.00008
4.430(7)	−0.00007(4)	0.00000(4)	−0.00005(3)	0.00012(11)	−0.00013(8)	0.00025(20)	−0.00012
5.129(8)	−0.00006(6)	−0.00003(5)	−0.00002(3)	0.00011(15)	−0.00011(10)	0.00023(29)	−0.00010
6.033(7)	0.00007(8)	0.00002(5)	0.00006(4)	−0.00016(23)	0.00015(12)	0.00034(45)	0.00015

Note: Two significant digits have been reported as uncertainties for the e_{11}, e_{22}, e_{33}, e_{13}, V_s, ε_s to evidence the expected evolution with pressure described by Angel (2000b).
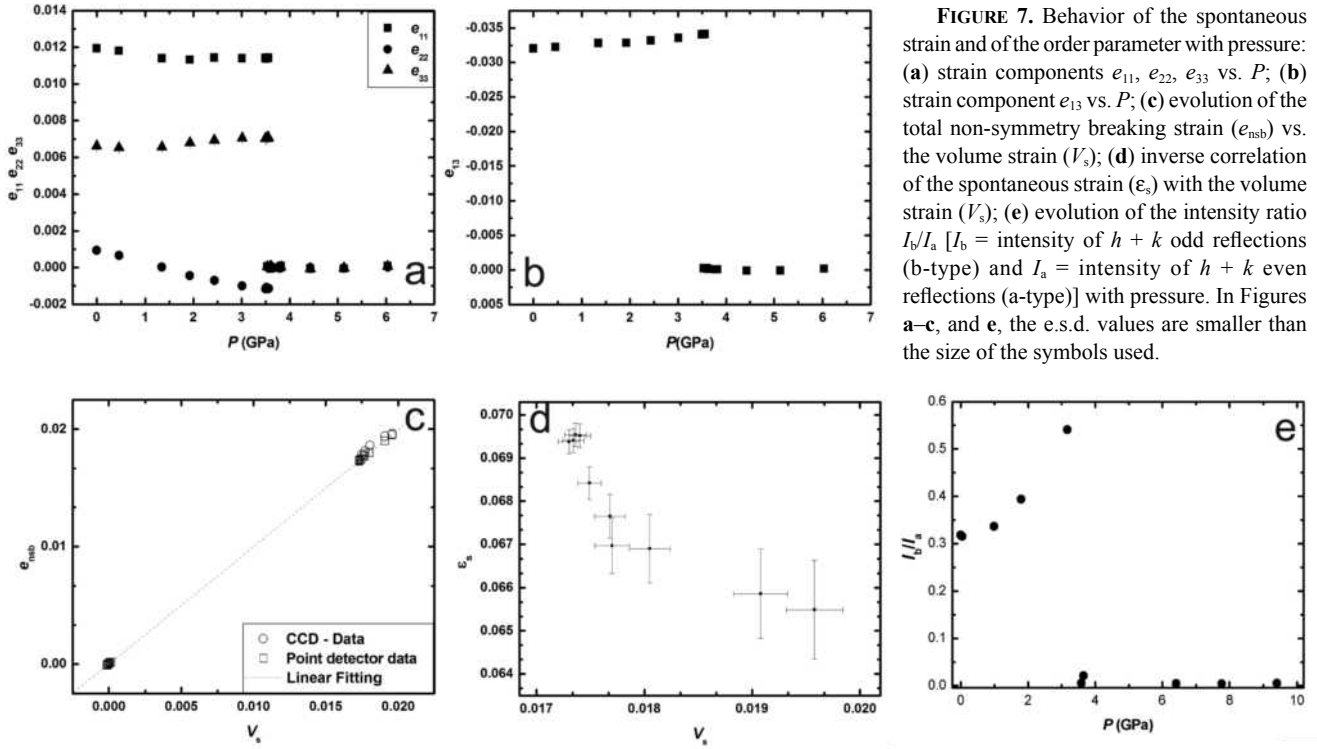* Data measured during decompression.

FIGURE 7. Behavior of the spontaneous strain and of the order parameter with pressure: (**a**) strain components e_{11}, e_{22}, e_{33} vs. P; (**b**) strain component e_{13} vs. P; (**c**) evolution of the total non-symmetry breaking strain (e_{nsb}) vs. the volume strain (V_s); (**d**) inverse correlation of the spontaneous strain (ε_s) with the volume strain (V_s); (**e**) evolution of the intensity ratio I_b/I_a [I_b = intensity of $h + k$ odd reflections (b-type) and I_a = intensity of $h + k$ even reflections (a-type)] with pressure. In Figures **a–c**, and **e**, the e.s.d. values are smaller than the size of the symbols used.

the two sets of values plot close to a straight line with slope equal to 1 (Fig. 7c), suggesting that the strain calculation is at least self consistent.

In the $P2_1/c$ to $C2/c$ high-pressure phase transition, the high- and low-symmetry phases are both monoclinic (point group $2/m$) and, therefore, the spontaneous strain associated with the transition is non-symmetry breaking and transforms as $\Gamma_{identity}$ (co-elastic behavior). The allowed coupling terms between strain and order parameter in the Landau expansion (Carpenter et al. 1998) are, hence, of the form e_iQ^2, with the assumption that higher order terms are usually negligible. This implies that Q^2 should scale with ε_s and with V_s as observed for other high-pressure (Boffa Ballaran et al. 2000), as well as for high-temperature (Cámara et al. 2003b), phase transformations of clinopyroxenes. However, in the case of the BTS-308 pigeonite of this study, an inverse relationship between scalar spontaneous strain and volume strain is observed. An unexpected behavior is also observed for the evolution of the I_b/I_a ratio (Fig. 7e), where I_b is the intensity of the *b*-type reflections ($h + k = 2n + 1$) present only in the *P*-symmetry and I_a is the intensity of $h + k = 2n$ reflections (*a*-type reflections). This quantity is usually used as proportional to the square of the order parameter (Q^2) (Bruce and Cowley 1981) describing a phase transformation, and as such it is expected to decrease as a function of pressure and to disappear at the transition. In contrast, the I_b/I_a ratio increases with pressure and abruptly disappears at the transition pressure. $P2_1/c$ pigeonite pyroxenes can be considered to be related either to a high-temperature form (Cámara et al. 2003b) or to the high-pressure form described in this paper. Both phases have space group $C2/c$, but distinct structures in terms of kinking of the tetrahedral chains. It has been shown that a HT $C2/c$

to $P2_1/c$ phase transformation occurs as a function of pressure in spodumene (Arlt and Angel 2000; Sondergeld et al. 2006), $LiScSi_2O_6$, and in $ZnSiO_3$ (Arlt and Angel 2000) and that for this transition the I_b/I_a ratio gives an internally consistent picture of the evolution of the $P2_1/c$ structure with pressure. The case of $ZnSiO_3$ clinopyroxene is particularly interesting because this material undergoes a further phase transition with increasing pressure from $P2_1/c$ to HP $C2/c$ (Arlt and Angel 2000). In this case, the I_b/I_a ratio, which is strictly zero in the pressure range of the HT $C2/c$ phase, becomes different from zero at the pressure of the HT $C2/c$ to $P2_1/c$ phase transformation and increases with pressure reaching a plateau before disappearing at the transition pressure of the $P2_1/c$ to HP $C2/c$ transformation (Fig. 2 in Arlt and Angel 2000). It is to be expected, therefore, that in the case of our sample, the behavior of the $P2_1/c$ to HP $C2/c$ transformation will be influenced by a possible HT $C2/c$ to $P2_1/c$ phase transformation [which has been observed at high temperature and room P, Cámara et al. (2002)], even if this one cannot be observed in the range of pressure measured. Indeed, Christy and Angel (1995) have suggested that the $P2_1/c$ polymorph can be considered as an ordered intergrowth of the two $C2/c$ polymorphs since the A chain is S-rotated and extended, with kinking O3-O3-O3 angles similar to the O-rotated chain of the HT phase (see Fig. 5a), and the B chain is O-rotated with kinking angles similar to the O-rotated chains of the high-pressure polymorph. In this sense, the low-P/low-T structure could be considered as an alternating ordered sequence of HP and HT sub-lattices in a "cell doubled" phase (Christy and Angel 1995). Therefore, two order parameters, Q_1 (HT-sub-lattice) and Q_2 (HP sub-lattice), will be associated to the two sub-lattices and, following Christy and Angel (1995), the corresponding Landau free energy expansion would be
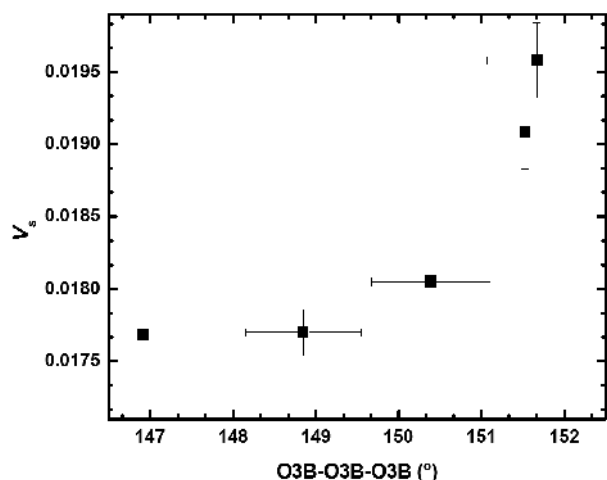
FIGURE 8. Evolution of the volume strain (V_s) plotted against the kinking angle of the B-chain (O3B-O3B-O3B). To calculate the strain volume at the pressures values at which full sets of intensity data have been collected with the CCD, because the unit-cell parameters obtained from measurements with a CCD lack the accuracy of data obtained from the eight-positions centering procedure, we have followed a slightly different procedure: instead of using the measured $P2_1/c$ lattice parameters, we have calculated them at each pressure of the CCD measurements using the $P2_1/c$ EoS parameters reported in Table 5 and used these calculated values to obtain the strain components according to Equation 1 in the text.

$$G = \frac{1}{2}\left\{ a\left(Q_1 + Q_2\right) + b\left(Q_1^2 + Q_2^2\right) + c\left(Q_1^3 + Q_2^3\right) + d\left(Q_1^4 + Q_2^4\right) \right\}$$
$$+ \left(\lambda/2\right)\left(Q_1 + Q_2\right)^2 \tag{2}$$

with the final term being the coupling energy between the two sub-lattices. Since both phase transformations are first order in character, higher order terms would be required, even if the basic behavior of the system described by Equation 2 were the same.

To model correctly the transition, we would thus need to choose a geometrical feature related to the variation of either Q_1 or Q_2 order parameters. From the data reported in Arlt and Angel (2000) we can assume the intensity of the b-type reflections as being proportional to Q_1^2, which would explain why they do not scale with the volume strain associated with the $P2_1/c$ to HP $C2/c$ phase transition. Instead a reasonable correlation between the volume strain associated with the $P2_1/c$ to HP $C2/c$ phase transition and the kinking of the B chain has been found (Fig. 8), suggesting that this geometrical parameter could be used as proportional to Q_2^2.

ACKNOWLEDGMENTS

REFERENCES CITED

Allan, D.R., Miletich, R., and Angel, R.J. (1996) A diamond-anvil cell for single crystal X-ray diffraction studies to pressures in excess of 10 GPa. Review of Scientific Instruments, 67, 840–842.

Angel, R.J. (2000a) Equations of state. In R.M. Hazen and R.T. Downs, Eds., High Temperature and High-Pressure Crystal Chemistry, 41, p. 117–211. Reviews in Mineralogy and Geochemistry, Mineralogical Society of America, Chantilly, Virginia.

——— (2000b) High-pressure structural phase transitions. In S.A.T. Redfern and M.A. Carpenter, Eds., Transformation Processes in Minerals, 39, p. 85–104. Reviews in Mineralogy and Geochemistry, Mineralogical Society of America, Chantilly, Virginia.

——— (2002) EOSFIT V5.2 program. Crystallography Laboratory, Virginia Tech, Blacksburg.

——— (2004) Absorption corrections for diamond-anvil pressure cells implemented in the software package—Absorb 6.0. Journal of Applied Crystallography, 37, 486–492.

Angel, R.J. and Hugh-Jones, D.A. (1994) Equations of state and thermodynamic properties of enstatite pyroxenes. Journal of Geophysical Research: Solid Earth, 99, 19777–19783.

Angel, R.J., Chopelas, A., and Ross, N.L. (1992) Stability of high-density clinoenstatite at upper-mantle pressures. Nature, 358, 322–324.

Angel, R.J., Allan, D.R., Miletich, R., and Finger, L.W. (1997) The use of quartz as an internal pressure standard in high-pressure crystallography. Journal of Applied Crystallography, 30, 461–466.

Angel, R.J., Downs, R.T., and Finger, L.W. (2000) High-temperature high-pressure diffractometry. In R.M. Hazen and R.T. Downs, Eds., High-Temperature and High-Pressure Crystal Chemistry, 41, p. 559–596. Reviews in Mineralogy and Geochemistry, Mineralogical Society of America and Geochemical Society, Chantilly, Virginia.

Arlt, T. and Angel, R.J. (2000) Displacive phase transitions in C-centered clinopyroxenes: Spodumene, LiScSi$_2$O$_6$ and ZnSiO$_3$. Physics and Chemistry of Minerals, 27, 719–731.

Arlt, T., Angel, R.J., Miletich, R., Armbruster, T., and Peters, T. (1998) High-pressure $P2_1/c$-$C2/c$ phase transitions in clinopyroxenes: Influence of cation size and electronic structure. American Mineralogist, 83, 1176–1181.

Balić-Žunić, T. and Vicković, I. (1996) IVTON-program for the calculation of geometrical aspects of crystal structures and some crystal chemical applications. Journal of Applied Crystallography, 29, 305–306.

Birch, F. (1947) Finite elastic strain of cubic crystals. Physical Review, 71, 809–824.

Boffa Ballaran, T., Angel, R.J., and Carpenter, M.A. (2000) High-pressure transformation behaviour of the cummingtonite-grunerite solid solution. European Journal of Mineralogy, 12, 1195–1213.

Bridgman, P.W. (1923) The compressibility of thirty metals as a function of pressure and temperature. Proceedings of the American Academy of Arts and Sciences, 58, 165–242.

Brown, J.M., Abramson, E.H., and Angel, R.J. (2006) Triclinic elastic constants for low albite. Physics and Chemistry of Minerals, 33, 256–265.

Bruce, A.D. and Cowley, R.A. (1981) Structural Phase Transitions. Taylor and Francis, London.

Burnham, C.W., Clark, J.R., Papike, J.J., and Prewitt, C.T. (1967) A proposed crystallographic nomenclature for clinopyroxene structures. Zeitschrift für Kristallographie, 125, 109–119.

Cámara, F., Carpenter, M.A., Domeneghetti, M.C., and Tazzoli, V. (2002) Non-convergent ordering and displacive phase transition in pigeonite: in situ HT XRD study. Physics and Chemistry of Minerals, 29, 331–340.

——— (2003a) Coupling between non-convergent ordering and transition temperature in the $C2/c \leftrightarrow P2_1/c$ phase transition in pigeonite. American Mineralogist, 88, 1115–1128.

Cámara, F., Iezzi, G., and Oberti, R. (2003b) HT-XRD study of synthetic ferrian magnesian spodumene: The effect of site dimension on the $P2_1/c \rightarrow C2/c$ phase transition. Physics and Chemistry of Minerals, 30, 20–30.

Carpenter, M.A., Salje, E.K.H., and Graeme-Barber, A. (1998) Spontaneous strain as a determinant of thermodynamic properties for phase transitions in minerals. European Journal of Mineralogy, 10, 621–691.

Christy, A.G. and Angel, R.J. (1995) A model for the origin of the cell-doubling phase-transitions in clinopyroxene and body-centered anorthite. Physics and Chemistry of Minerals, 22, 129–135.

Domeneghetti, M.C., Zema, M., and Tazzoli, V. (2005) Kinetics of Fe^{2+}-Mg order-disorder in $P2_1/c$ pigeonite. American Mineralogist, 90, 1816–1823.

Downs, R.T. (2003) Topology of the pyroxenes as a function of temperature, pressure, and composition as determined from the pro-crystal electron density. American Mineralogist, 88, 556–566.

Hugh-Jones, D.A. and Angel, R.J. (1994) A compressional study of MgSiO$_3$ orthoenstatite up to 8.5 GPa. American Mineralogist, 79, 405–410.

Hugh-Jones, D.A., Woodland, A.B., and Angel, R.J. (1994) The structure of high-pressure $C2/c$ ferrosilite and crystal-chemistry of high-pressure $C2/c$ pyroxenes. American Mineralogist, 79, 1032–1041.

Johnson, E. (2007) Elastic behavior of intermediate plagioclase at high pressure. The 12th Annual Geosciences Student Research Symposium, Virginia Tech, p. 25.

King, H.E. and Finger, L.W. (1979) Diffracted beam crystal centering and its application to high-pressure crystallography. Journal of Applied Crystallography, 12, 374–378.

McCarthy, A.C., Downs, R.T., and Thompson, R.M. (2008) Compressibility trends of the clinopyroxenes, and in situ high-pressure single-crystal X-ray diffraction study of jadeite. American Mineralogist, 93, 198–209.

Miletich, R., Allan, D.R., and Kuhs, W.F. (2000) High-pressure single-crystal techniques. In R.M. Hazen and R.T. Downs, Eds., High-Temperature and High-Pressure Crystal Chemistry, 41, p. 445–519. Reviews in Mineralogy and Geochemistry, Mineralogical Society of America, Chantilly, Virginia.

Nestola, F., Tribaudino, M., and Boffa Ballaran, T. (2004) High-pressure behavior, transformation, and crystal structure of synthetic iron-free pigeonite. American Mineralogist, 89, 189–196.

Nestola, F., Boffa Ballaran, T., Balić-Žunić, T., Secco, L., and Dal Negro, A. (2008a) The high-pressure behavior of an Al- and Fe-rich natural orthopyroxene. American Mineralogist, 93, 644–652.

Nestola, F., Boffa Ballaran, T., Liebske, C., Thompson, R., and Downs, R.T. (2008b) The effect of the hedenbergitic substitution on the compressibility of jadeite. American Mineralogist, 93, 1005–1013.

Nestola, F., Boffa Ballaran, T., and Ohashi, H. (2008c) The high-pressure $C2/c$-$P2_1/c$ phase transition along the $LiAlSi_2O_6$-$LiGaSi_2O_6$ solid solution. Physics and Chemistry of Minerals, 35, 477–484.

Ohashi, Y. (1972) Program strain. Program listing provided in Hazen and Finger (1982) Comparative crystal-chemistry. Wiley, New York.

Ohashi, H., Fujita, T., and Osawa, T. (1982) Crystal structure of sodium titanium silicate ($NaTiSi_2O_6$) pyroxene. Journal of the Japanese Association of Mineralogy, Petrology and Economic Geology, 77, 305–309.

Pasqual, D., Molin, G., and Tribaudino, M. (2000) Single-crystal thermometric calibration of Fe-Mg order-disorder in pigeonites. American Mineralogist, 85, 953–962.

Ralph, R.L. and Finger, L.W. (1982) A computer program for refinement of crystal orientation matrix and lattice constraints from diffractometer data with lattice symmetry constraints. Journal of Applied Crystallography, 15, 537–539.

Robinson, K., Gibbs, G.V., and Ribbe, P.H. (1971) Quadratic elongation: a quantitative measure of distortion in coordination polyhedra. Science, 172, 567–570.

Ross, N.L. and Reynard, B. (1999) The effect of iron on the $P2_1/c$ to $C2/c$ transition in (Mg,Fe)SiO_3 clinopyroxenes. European Journal of Mineralogy, 11, 585–589.

Salje, E.K.H. (1991) Crystallography and structural phase-transitions, an introduction. Acta Crystallographica, A47, 453–455.

Schlenker, J.L., Gibbs, G.V., and Boisen, M.B. (1978) Strain-tensor components expressed in terms of lattice-parameters. Acta Crystallographica, A34, 52–54.

Secco, L. (1988) Crystal-chemistry of high-pressure clinopyroxene from spinel lherzolite nodules Mts. Leura and Noorat Suites, Victoria, Australia. Mineralogy and Petrology, 39, 175–185.

Sheldrick, G.M. (1998) Programs for crystal structure analysis (Release 97-2). University of Göttingen, Germany.

Sondergeld, P., Li, B., Schreuer, J., and Carpenter, M.A. (2006) Discontinuous evolution of single-crystal elastic constants as a function of pressure through the $C2/c \leftrightarrow P2_1/c$ phase transition in spodumene ($LiAlSi_2O6$). Journal of Geophysical Research, 111, B07202, DOI: 10.1029/2005JB004098.

Stoe and Cie (1999) Crystal Optimization for Numerical Absorption Correction. Stoe and Cie GmbH, Darmstad, Germany.

——— (2001) Data Reduction Program. Stoe and Cie GmbH, Darmstad, Germany.

Thompson Jr., J.B. (1970) Geometrical possibilities for amphiboles structures: model biopyriboles. American Mineralogist, 55, 292–293.

Thompson, R.M. and Downs, R.T. (2008) The crystal structure of diopside at pressure to 10 GPa. American Mineralogist, 93, 177–186.

Tribaudino, M. and Nestola, F. (2002) Average and local structure in $P2_1/c$ clinopyroxenes along the join diopside-enstatite (CaMgSi$_2$O$_6$-Mg$_2$Si$_2$O$_6$). European Journal of Mineralogy, 14, 549–555.

Tribaudino, M., Prencipe, M., Nestola, F., and Hanfland, M. (2001) A $P2_1/c$-$C2/c$ high-pressure phase transition in Ca$_{0.5}$Mg$_{1.5}$Si$_2$O$_6$ clinopyroxene. American Mineralogist, 86, 807–813.

Tribaudino, M., Nestola, F., Cámara, F., and Domeneghetti, M.C. (2002) The high-temperature $P2_1/c$-$C2/c$ phase transition in Fe-free pyroxene (Ca$_{0.15}$Mg$_{1.85}$Si$_2$O$_6$): Structural and thermodynamic behavior. American Mineralogist, 87, 648–657.

Ullrich, A. and Miletich, R. (2008) Elastic properties of clinopyroxenes: Nonlinear lattice elasticity at high-pressure transformations. Geophysical Research Abstracts, 10, EGU2008-A-10452.

Wilson, A.J.C. (1995) International Tables for Crystallography. Volume C. Kluwer Academic Publishers, Dordrecht.

Zhang, L., Ahsbahs, H., Hafner, S.S., and Kutoglu, A. (1997) Single-crystal compression and crystal structure of clinopyroxene up to 10 GPa. American Mineralogist, 82, 245–258.